Very-high-cycle fatigue behavior of AlSi10Mg manufactured by selected laser melting: Crystal plasticity modeling

Wenjie Zhang [a], Yanying Hu [a], Xianfeng Ma [a,*], Guian Qian [b,c,*], Jiamei Zhang [b,c], Zhengmao Yang [b], Filippo Berto [d]

[a] Sino-French Institute of Nuclear Engineering and Technology, Sun Yat-Sen University, Zhuhai 519082, Guangdong, China
[b] State Key Laboratory of Nonlinear Mechanics (LNM), Institute of Mechanics, Chinese Academy of Sciences, Beijing 100190, China
[c] School of Engineering Science, University of Chinese Academy of Sciences, Beijing 100049, China
[d] Department of Mechanical and Industrial Engineering, Norwegian University of Science and Technology (NTNU), Richard Birkelands vei 2b, 7491 Trondheim, Norway

ABSTRACT

The high-cycle and very-high-cycle fatigue (VHCF) behaviors of AlSi10Mg alloy produced by additive manufacturing (AM) were studied. A crystal plasticity finite element model (CPFEM) with Voronoi tessellation was developed to simulate the cyclic plastic deformation considering defect effects. Morrow's model and Smith-Watson-Topper (SWT) model were used to predict the fatigue life and the SWT model was in good agreement with the experimental life between 10^5 and 10^9. CPFEM simulation indicated that the accumulated cyclic plastic strain is significantly increased near a pore than that of an inclusion. The residual stress near an inclusion led to large plastic strain localization, which is harmful to fatigue performance.

1. Introduction

Selective laser melting (SLM) has become a popular additive manufacturing (AM) technology in recent years due to the advantages of less waste of material and feasibility for variable shape designs [1,2]. SLM has been widely applied to the manufacture of advanced alloys, such as titanium alloys [3,4] and aluminum alloys [5–7]. It is known that the quality of these products made by SLM is remarkably dependent on the process parameters. Recently, some interesting results [8–10] has been reported on the interrelationship between the microstructure features (e.g. defects including internal porosity, oxide inclusions, grain size, and surface roughness) and the mechanical performances (e.g. tensile and fatigue properties) of the products made by SLM.

With the increasing demands of safety requirements, more and more engineering components are designed to endure a fatigue life of more than 10^7 cycles, even up to 10^8 and 10^9 cycles. It is well known as the very-high-cycle fatigue (VHCF) [11]. The research on VHCF can be traced back to the study on the fatigue characteristics of mild steel over 10^9 cycles by Kikukawa et al [12]. In the year of 1982, the concept of VHCF was firstly proposed by Wells [13]. Ever since then, numerous researchers have been engaged in the study of VHCF behavior and

failure mechanism. Lankford and Kusenberger [14] found that the crack initiation stage occupied a large proportion of the total fatigue life. Asami and Emura [15], Sakai et al. [16], and Hong et al. [17] studied the fracture surface characteristics of specimens failed in the VHCF regime. Among the models to explain the initiation of VHCF cracks, the numerous cyclic pressing model (NCP model) is one of the most well-known methods, which is proposed by Hong et al. [18]. In the high-cycle fatigue (HCF) and VHCF regimes, 80–90% of fatigue life would be consumed in the crack initiation stage [19], so the crack initiation process played an important role in the fatigue property. It is well known that the crack initiation process highly depends on the microstructure of material and especially the local defects. Unfortunately, defect-free SLM product has not been developed yet [20]. In addition, very few studies have been reported on the VHCF behavior of additively manufactured alloys. Thus, it is important to study the effect of defects on the local plasticity behavior and fatigue life in VHCF regime.

It is not appropriate to assume the material as a homogeneous medium for HCF failure and especially VHCF failure, because the fatigue crack initiation process is closely related to the local microstructural inhomogeneity, such as defects, in the material. In a polycrystalline material, it is usually composed of grains in different orientations,

inclusions and pores etc. As a powerful modeling method on the microscopic scale, crystal plasticity finite element model (CPFEM) has been widely used to analyze the mechanical properties of alloys in which the plastic deformation is by dislocation slip or twinning of crystals. The crystal plasticity theory can not only predict the localized stress and strain characteristics on a grain-to-grain level, but also the macroscopic mechanical properties of the material with considerable number of grains. Hence, this method has been increasingly used in the study of VHCF behavior in recent decades. McDowell et al. [21] have applied the CPFEM to investigate the plastic behavior and fatigue properties of Al 7056-T6 [21], Ti-6Al-4V [22,23], and Mo-Si-B alloys [24]. They suggested multiple failure mechanisms and fatigue indicator parameters (FIPs) which should be considered in the experimental and modeling study in the HCF and VHCF regimes [25]. Han and Yang et al. [26] applied CPFEM to characterize the damage mechanism of surface crack initiation and internal crack initiation behavior. It is a good way to use CPFEM to study the VHCF issue of SLM product by taking into account the effects of microstructure features. In contrast, few studies have provided deep insights into the residual stress around inclusion during cooling process of SLM and the quantitative effects on fatigue life, although preliminary studies [27] indicated its effects on the plastic strain accumulation and fatigue crack initiation.

In this study, the cyclic plasticity behaviors and fatigue life prediction of AlSi10Mg alloy fabricated by selective laser melting have been studied. A CPFEM with user-developed Voronoi tessellation was used to predict fatigue life and analyze the influence of defects and residual stress on the VHCF behavior. The results would provide reference for the evaluation of fatigue performance for SLMed AlSi10Mg alloy.

2. Material and simulation methods

2.1. Material and experimental

The alloy used in the present study is an AlSi10Mg alloy fabricated by SLM. The nominal chemical composition of AlSi10Mg alloy is listed in Table 1. The specimens were manufactured by the SLM process, and the geometry dimensions were shown in Fig. 1. The initial microstructure of the present AlSi10Mg alloy was shown in Fig. 2. The electron back-scattering diffraction (EBSD) results showed almost equiaxed grains with an average grain size of 20–25 μm in this case. The microstructure did not show evident texture. It is known that AlSi10Mg alloy has a face center cubic (FCC) structure [28]. Hence, the dislocation glide was assumed to occur on 12 possible slip systems (four {1 1 1} slip planes, three $\langle 1\,1\,0 \rangle$ slip directions) in AlSi10Mg alloy.

For the AlSi10Mg alloy, standard tensile specimens were machined and tensile tests were conducted under a strain rate of 10^{-3}/s. Representative tensile results of AlSi10Mg alloys were shown in Fig. 3. The AlSi10Mg alloy showed evident strain hardening behavior after yielding. In Fig. 3, the yield strength and ultimate tensile strength of AlSi10Mg alloy are measured to be 270 MPa and 465 MPa, respectively.

2.2. Crystal plasticity theory

In a classical crystal plasticity theory, the total deformation of a crystalline material consists of two parts: elastic deformation and inelastic deformation. Therefore, the total crystal deformation gradient $\boldsymbol{F}$ can be expressed as
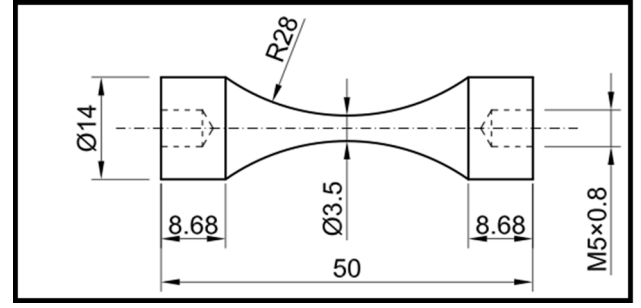
$$\boldsymbol{F} = \boldsymbol{F}^* \cdot \boldsymbol{F}^P \tag{1}$$

Fig. 1. The shape and dimensions of fatigue specimens (in mm).

where $\boldsymbol{F}^*$ represents the elastic deformation gradient and $\boldsymbol{F}^P$ the plastic deformation gradient.

For AlSi10Mg alloy, the plastic deformation is primarily caused by dislocation slip, especially via the octahedral $\{1\,1\,1\} \langle 1\,1\,0 \rangle$ slip systems. The plastic velocity gradient can be expressed as the sum of the shear strain rates in all slip systems:

$$\boldsymbol{L}_P = \sum_{\alpha=1}^{n} \dot{\gamma}_\alpha \boldsymbol{s}_\alpha \otimes \boldsymbol{m}_\alpha \tag{2}$$

where n is the amount of slip systems, $\dot{\gamma}_\alpha$ is the shear strain rate for slip system α, $\boldsymbol{s}_\alpha$ and $\boldsymbol{m}_\alpha$ are respectively the unit vectors in the slip direction and normal to the slip plane for slip system α. The shear strain rate $\dot{\gamma}_\alpha$ is given as:

$$\dot{\gamma}_\alpha = \dot{\gamma}_0 \left(\frac{\tau_\alpha}{g_\alpha}\right) \left|\frac{\tau_\alpha}{g_\alpha}\right|^{n-1} \tag{3}$$

where g_α is the strain hardening function of the slip system α, $\dot{\gamma}_0$ is the reference shear strain rate, n is the sensitive coefficient of strain rate, τ_α is the cutting stress of slip system α. Considering that the kinematic hardening of this alloy under cyclic loading was not pronounced, so the back stress was not included in Eq. (3), according to the experimental studies of AlSi10Mg alloy in literature [29,30]. This model has been widely used to study the strain hardening behavior of similar alloys [31]. The crack initiation and short crack behaviors could also be properly modeld by this method [32,33]. There are also previous studies on crystal plasticity modeling of fatigue behavior of alloys, for instance, Proundhon et al. [34], Rovineli et al. [35], and Yue [36] etc., which did not take into account the kinematic hardening when it is not significant. Hence, the classical crystal plasticity model as Eq. (3) was adopted in the present study. The hardening function g_α is assumed to be related to the total slip γ in all slip systems:

$$g_\alpha = g_\alpha(\gamma) \tag{4}$$

$$\gamma = \sum_{\alpha=1}^{n} |\gamma_\alpha| \tag{5}$$

The strain hardening law of a single crystal is given as:

$$\dot{g}_\alpha = \sum_{\beta=1}^{n} h_{\alpha\beta} |\dot{\gamma}_\beta| \tag{6}$$

where $h_{\alpha\beta}$ is the matrix for hardening modulus. $h_{\alpha\beta}$ is given by:

$$h_{\alpha\beta} = qh + (1-q)h\delta_{\alpha\beta} \tag{7}$$

Table 1
Nominal chemical composition of AlSi10Mg alloy.

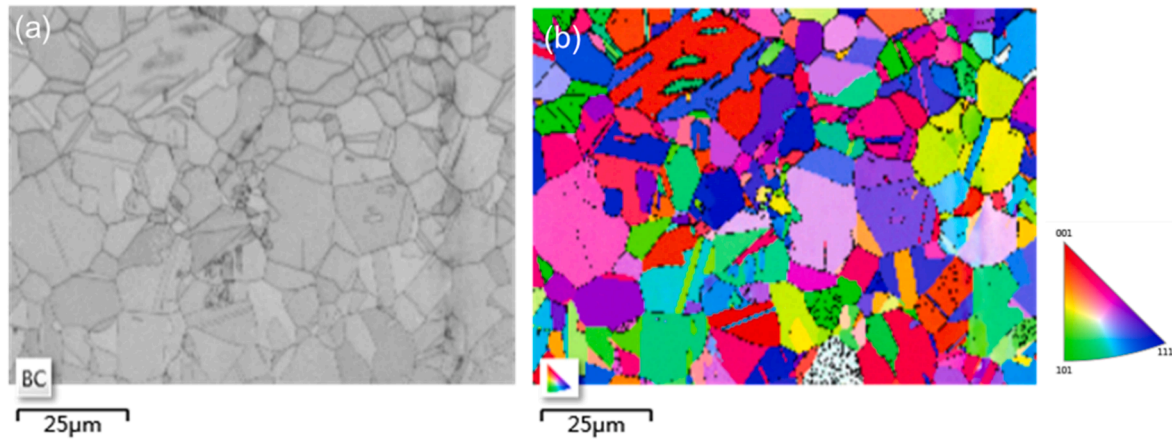| Al	Si	Mg	Fe	Ti	Cu	Cr	Mn	Ni
Bal.	9.75	0.22	0.092	0.011	<0.01	<0.01	<0.01	<0.01

Fig. 2. The initial microstructure of AlSi10Mg alloy: (a) grain morphology; (b) (Inverse pole figure) IPF grain orientation map.

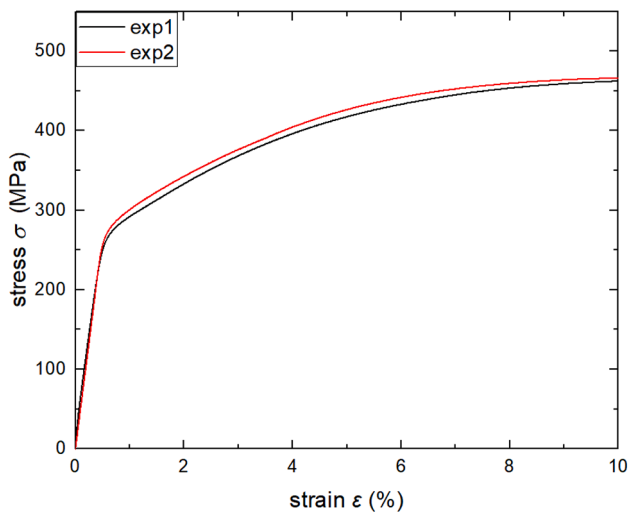**Fig. 3.** Tensile stress–strain curves of two AlSi10Mg alloy specimens.

$$h(\gamma) = h_0 \mathrm{sech}^2 \left| \frac{h_0 \gamma}{\tau_s - \tau_0} \right| \tag{8}$$

where q is the ratio of self-hardening effect to latent hardening effect, and the value is 1 or 1.4. h_0 is the initial hardening rate, τ_0 is the yield shear stress, and τ_s is the saturated flow stress.

3. Crystal plasticity finite element simulation

3.1. Finite element modeling

The finite element model of AlSi10Mg alloy is shown in Fig. 4. The height, width and thickness of the geometry model is 500 µm, 500 µm, and 20 µm, respectively, as shown in Fig. 4(a). The polycrystalline grain structure was created by a user-developed Python code based on Voronoi tessellation. The grain size was generated between 20 and 40 µm according to the experimental observation, following an average grain size of 20–25 µm, as shown in Fig. 4(b). The grain size distribution was in accordance with that obtained from metallographic examination. 320 grains were generated in the model, which was then meshed to compose of 7216 elements and 11,163 nodes. The grain orientations were randomly generated, to be consistent with the weak texture of AlSi10Mg alloy suggested by EBSD. In Fig. 4(a), the node at the bottom-left corner was constrained in X, Y and Z directions to prevent rigid body motion. The other nodes at the bottom were fixed in the Y direction, to allow

motion in the X direction. The Z direction of the plate was set to be free. The left and right sides of the model are also rationale to be set traction-free, similar to those shown in the previous studies. C3D8I elements of the finite element software ABAQUS were used in the simulation. A uniaxial load was applied at the upper boundary of the model along vertical (Y-axis) direction to simulated uniaxial tensile tests at a strain rate of 0.001 s^{-1}.

3.2. Cyclic plasticity simulation

Uniaxial cyclic loading was performed at the upper boundary of the finite element model in Fig. 4. The method of displacement control was used in the simulation, expressed as

$$U_2(t) = U_{2,0} \times Amplitude(t) \tag{9}$$

where $U_{2,0}$ is a constant, different $U_{2,0}$ values represent different strain or strain amplitudes. $Amplitude(t)$ is a function of triangular wave with unit amplitude, to define uniaxial tension and compression loading versus time. As suggested by previous studies [37], the cyclic frequency in the simulation is lower than that in an ultrasonic fatigue test (20 kHz) due to the latter is difficult to be implemented in the crystal plasticity simulation. Moreover, it is indicated that frequency effect on fatigue life is less significant in fcc alloys than that of bcc alloys. For instance, fatigue tests showed little effect of cyclic frequency on the fatigue life of superalloys in the 10^6–10^9 cycles regime at room temperature [38]. Caton and Allison et al [39] also reported that there was no influence of loading frequency on the HCF behavior of cast aluminum alloy 319 at room temperature. It is reasonable that according to the study of McDowell et al. [37] on the HCF-VHCF transition and strain localization behavior of alloys, a cyclic frequency of 1 Hz was used in the present crystal plasticity simulation. Note that in the present study, the peak stress applied in fatigue tests were mostly lower than the yield stress (~270 MPa) except for a few samples at R = 0.5, hence the majority of strain levels were calculated within the scope of elasticity and the associated rate effect was small.

3.3. Calibration of model parameters

The crystal plasticity model has been implemented in ABAQUS via a user-defined material subroutine (UMAT), which has been successfully applied in the cyclic plasticity behavior of nickel-based superalloys [31] and zirconium alloys [33]. The crystal orientation of each grain was defined following a random texture, to be consistent with the weak texture indicated by the EBSD result in Fig. 2. The Euler angle data of grain orientation and grain morphology was generated by a Python code developed by the authors. For AlSi10Mg alloy, it has three independent elastic constants due to the face center cubic symmetry. The elastic
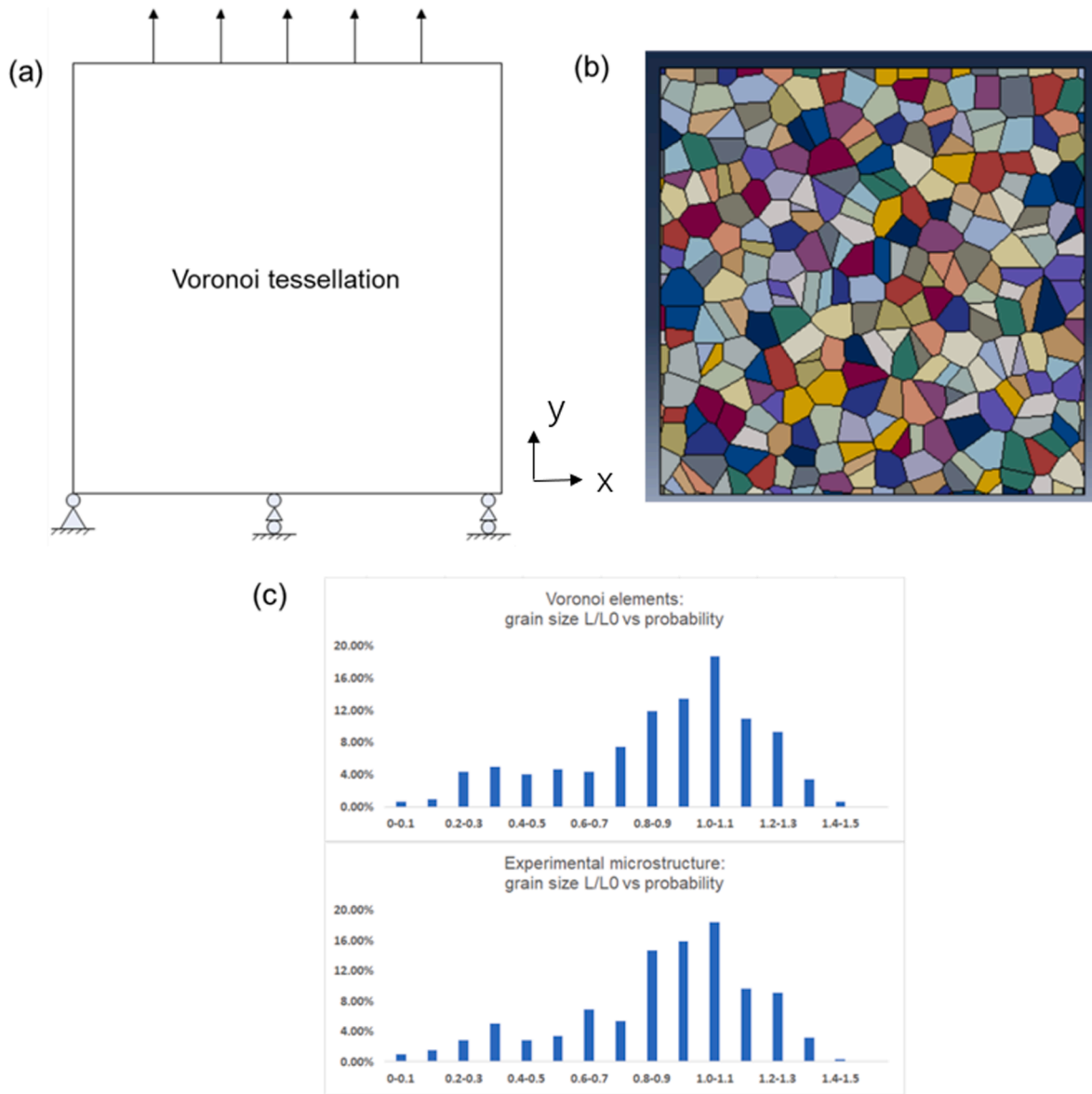
Fig. 4. Crystal plasticity finite element model of AlSi10Mg alloy implemented in ABAQUS software: (a) geometry model and boundary condition; (b) grain aggregates created by a user-developed Python code based on Voronoi tessellation; (c) grain size distribution in accordance with the experimental microstructure.

parameters used in this study were shown in Table 2. Note that in the simulation of the tensile stress–strain curves, the strain rate was kept at 10^{-3} s^{-1} by displacement control, which is consistent with the tensile test. In the present study, n is taken as 10 to best fit the experimental tensile stress–strain curves as well as depict the rate sensitivity. It is close the value of $n = 7.14$ that was used in the simulation study of AA7075 alloy [40]. C_{11}, C_{12} and C_{44} represent the three elastic constants. The other model parameters are mentioned in the Section 2.2 of crystal plasticity theory.

The simulation of uniaxial tension of the AlSi10Mg specimen was performed using the finite element geometry model in Fig. 4. The calibration of crystal plasticity model parameters were conducted following the try-and-error method by comparing with the tensile stress–strain curves of AlSi10Mg alloy in Fig. 3. For each of the simulation, 320 grains with different grain orientation and morphology was generated, following the same average grain size and the same set of crystal plasticity model parameters. It is consistent with the simulation studies of McDowell et al. [29] and Cailletaud et al. [41] that grain number of 250 or above was needed to provide stress–strain curves without evident scattering in a Voronoi polycrystalline aggregate. The difference between the curves of ten simulations was less than 2% when the strain was in the range of 0–6%. The average stress–strain curve obtained in multiple simulations is shown in Fig. 5. It is seen that the tensile curve simulated by crystal plasticity model coincided well with the experimental ones.

Table 2
Elasticity and crystal plasticity model parameters of AlSi10Mg alloy.

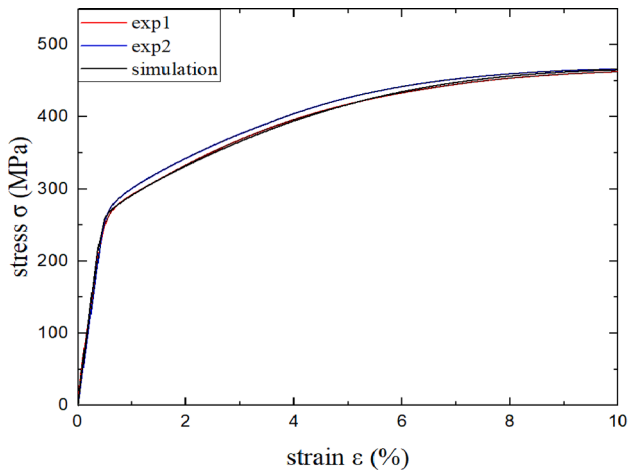| C_{11}/MPa	C_{12}/MPa	C_{44}/MPa	$\dot{\gamma}_0$	n	h_0/MPa	τ_s/MPa	τ_0/MPa	q
90,731	51,345	24,087	0.001	10	220	74	42	1

Fig. 5. The stress–strain curves of AlSi10Mg alloy by crystal plasticity simulation in comparison with the experimental result.

3.4. Voronoi modeling of a representative area element

To investigate the effects of defects, i.e. pores and inclusions, on the fatigue behavior of SLMed AlSi10Mg alloy, Voronoi aggregate model with a pore or an inclusion was established. As shown in Fig. 6(a), there is a pore with a diameter of 70 μm at the center of the Voronoi grains, which is obtained by measuring the size of the lack of fusion region from the metallographic images of SLMed AlSi10Mg alloy. Regarding the effect of inclusion, Voronoi model with an inclusion was generated, as shown in Fig. 6(b). A circular inclusion with a diameter of 50 μm was surrounded by multiple grains, as shown inFig. 6(b). The dimension came from the statistical average value from experimental micrographs. According to the experimental characterization by scanning elctron microscopy (SEM) and energy dispersive spectrometer (EDS) analyses, the inclusions in AlSi10Mg alloy are mainly Al_2O_3, with elastic modulus $E = 370$ GPa and Poisson ratio $\mu = 0.22$. There was no evident interfacial gap between Al_2O_3 inclusion and the matrix. Hence the inclusion is assumed to be perfectly bonded with the matrix. Cyclic tension–compression load was applied at the upper boundary of the polycrystal finite element model along the vertical (y-axis) direction, as shown in Fig. 4 and Fig. 6.
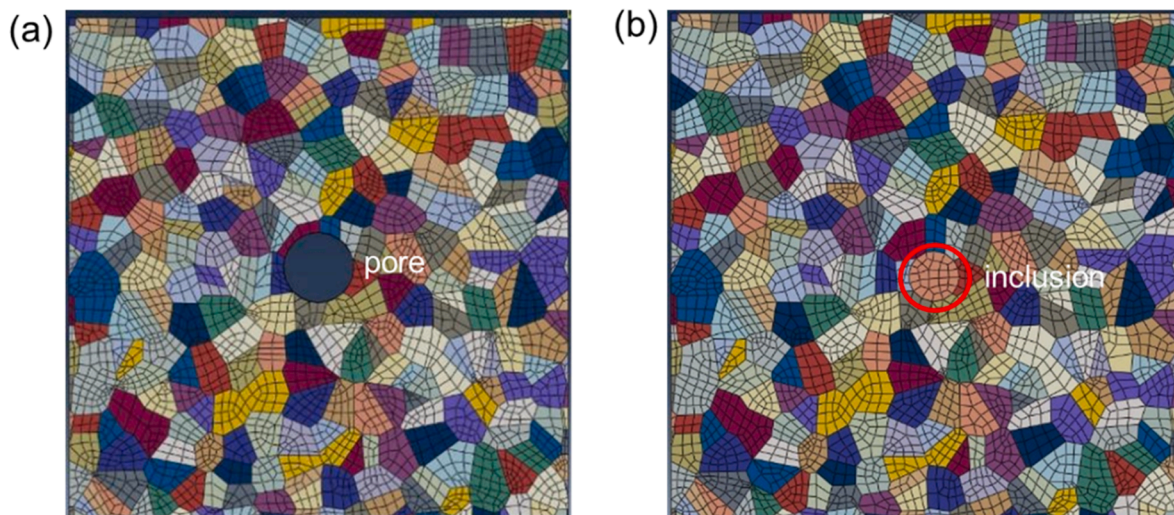
3.5. Residual stress by cooling down of Voronoi model with an inclusion

Besides the mechanical inhomogeneity of inclusions, the difference in thermal properties also makes additional contribution to its influence on the fatigue property of AlSi10Mg alloy. It is known that residual stresses would be generated in the AlSi10Mg alloys during the layer-by-layer printing process. Residual stress was mostly introduced in the alloy by cooling down. By setting the thermal expansion coefficient of the alloy and reducing the temperature of the whole model, residual stresses emerged around the inclusion. The thermal expansion coefficient of AlSi10Mg alloy is set as 22.9 μm/(m·°C), and the thermal expansion coefficient of Al_2O_3 inclusions is taken as 5.5 μm/(m·°C). The CPFEM of Voronoi grains with an embedded inclusion is shown in Fig. 6 (b). The cooling process is implemented as a thermal step in ABAQUS to introduce residual stresses before the cyclic loading.

4. Results and discussion

4.1. Fatigue life prediction with SWT and Morrow's models

Finite element simulation was performed based on the crystal plasticity UMAT subroutine and Voronoi model shown in Fig. 4. Different strain amplitudes were applied to the upper boundary of Voronoi model to study the plastic deformation. In order to predict the fatigue life, the stress and strain on the upper boundary of representative volume element (RVE) were recorded and the simulation continued until the stress strain curve became stabilized. The stress–strain behavior of the alloy under cyclic loading was studied. The stress–strain hysteresis curves under different strain amplitudes by crystal plasticity simulation are shown in Fig. 7. The modulus result is given by $E = 60.37$ GPa, which is close to the experimental values in the tensile tests. It is seen that for the strain amplitude of 2%, the stress got stable at about 470 MPa after a few cycles. For the high cycle fatigue tests performed in this study, the strain amplitudes cannot be directly measured during the test. Nevertheless, the simulated stress–strain curves in Fig. 7 and Fig. 8(b) were comparable to the experimental results of AlSi10Mg alloy by Cai et al. [29]. For instance, at the strain amplitude of 0.3%, the stress amplitude predicted by the present crystal plasticity simulation was 195 MPa, which is close to 205 MPa by Cai's experimental result [29].

The last stable and closed stress–strain loop for each strain amplitude was analyzed by the calibrated crystal plasticity simulation, shown in Fig. 8(a). Each loop was called a hysteresis loop. The relationship between the vertices of the hysteresis loops in steady-state reflected the response of the stress amplitude σ_a under different strain amplitudes ε_a.

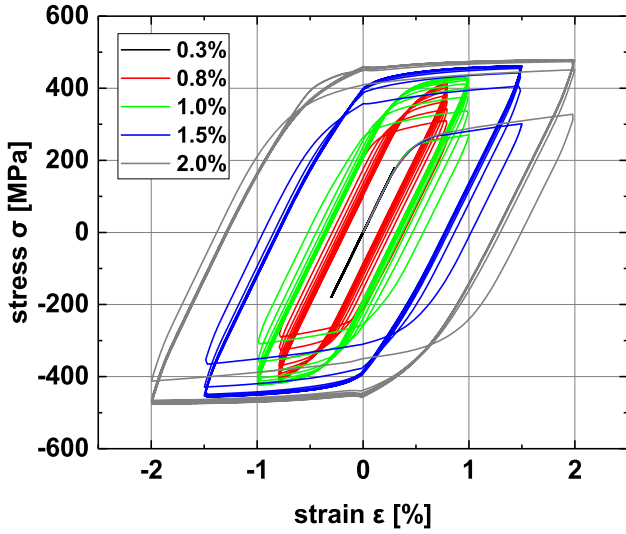**Fig. 6.** (a) Voronoi model with a pore (b) Voronoi model with an inclusion.

Fig. 7. The simulated cyclic stress–strain curves of AlSi10Mg alloy under different strain amplitudes.

The curve is shown in Fig. 8(b) and called the cyclic stress–strain curve, which is represented by the Ramberg-Osgood relationship:

$$\epsilon_a = \epsilon_{ea} + \epsilon_{pa} = \frac{\sigma_a}{E} + \left(\frac{\sigma_a}{K}\right)^{1/n} \tag{10}$$

where ϵ_{ea} is the elastic strain and ϵ_{pa} is the plastic strain under cyclic loads. E is the elastic modulus; K is cyclic strength coefficient; n is cyclic strain hardening coefficient, which is dimensionless. These parameters were determined by curve fitting method from the crystal plasticity simulation results in Fig. 8(b), which yielded the result of $E = 60.37$ GPa, $K = 467$ MPa, $n = 0.07$.

The elastic modulus obtained in the two tensile tests is 60.92 GPa and 62.59 GPa, respectively. Hence, it is seen that the simulated results by Eq. (10) are in good agreement with the experimental ones.

In the high cycle fatigue tests, the authors have performed three groups of fatigue tests and obtained the experimental data at $R = -1$, 0, and 0.5. Note that the strain range cannot be measured from the present fatigue test. Instead, the strain amplitude was calculated using the Ramberg-Osgood relationship of Eq. (10), for each stress level. For $R = -1$ test, the strain amplitude ϵ_a is equal to the peak strain or the maximum strain. Then, the strain amplitude, the stress level, and the corresponding fatigue life data of $R = -1$ was used to fit the following strain-life relationship:

$$\epsilon_a = \frac{\sigma_f'}{E}\left(2N_f\right)^b + \epsilon_f'\left(2N_f\right)^c \tag{11}$$

where σ_f' is the fatigue strength coefficient of stress dimension; the fitting value E in the previous section is 60.37 MPa; b is the fatigue strength exponent; ϵ_f' is the fatigue ductility coefficient; c is the fatigue ductility exponent. The values of these parameters are: $\sigma_f' = 38049.3$ MPa, $\epsilon_f' = 10.04616\%$, $b = -0.06886$, $c = -0.9802$.

As is shown above that the fatigue life data of $R = -1$ was applied to Eqs. (11)–(13) to fit the model parameters in Eqs. (11)–(13), herein the fatigue test data of $R = 0$ and 0.5 would be used to validate the obtained strain-life relationship. The well-known strain-life relationships considering mean stress effects are the Morrow's mean stress correction and the Smith-Watson-Topper model (SWT model). Morrow considered the mean stress and modified the formula as follows

$$\epsilon_a = \frac{\sigma_f' - \sigma_m}{E}\left(2N_f\right)^b + \epsilon_f'\left(2N_f\right)^c \tag{12}$$

where σ_m is mean stress. The modified formula of SWT model is

$$\sigma_{max}\epsilon_a = \frac{\left(\sigma_f'\right)^2}{E}\left(2N_f\right)^{2b} + \sigma_f'\epsilon_f'\left(2N_f\right)^{b+c} \tag{13}$$

where $\sigma_{max}\epsilon_a$ is called the SWT factor and it is constant for a given fatigue life. The fatigue life obtained in the fatigue tests were compared with the results predicted by Morrow's model and SWT model respectively, as shown in Fig. 9 (a) and (b).

It is shown that when the fatigue life is less than 10^9 cycles, most of the data points are located within the scatter band between the two dotted lines of $N_f/2$ and $2N_f$. It means that the fatigue life prediction by both Morrow's model (Fig. 9(a)) and SWT model (Fig. 9(b)) are satisfactory. Fig. 9(c) is a plot of the experimental peak stress versus the fatigue life for different specimens. There is a descending trend in the slope of data points for R = 0.5, R = 0, and R = −1 in Fig. 9(c), indicating that higher mean stress has evident effect on the fatigue life. All the experimental data of stress versus fatigue life in the present study was shown in Table 3.

Note that in Fig. 9(a), for Specimens A_1 and B_1, the predicted fatigue life had large dispersion from the experiment fatigue life. Note that Specimen A_2 and A_1 were tested under the same stress amplitude, and Specimen B_2 and B_1 were tested under the same stress amplitude. Moreover, satisfactory fatigue life prediction was obtained for Specimen A_2 and B_2 in Fig. 9(a). Hence, the deviation at Specimens A_1 and B_1 was probably due to the variation of microstructural defects which caused the large scattering of fatigue life. In details, the fracture surfaces of the
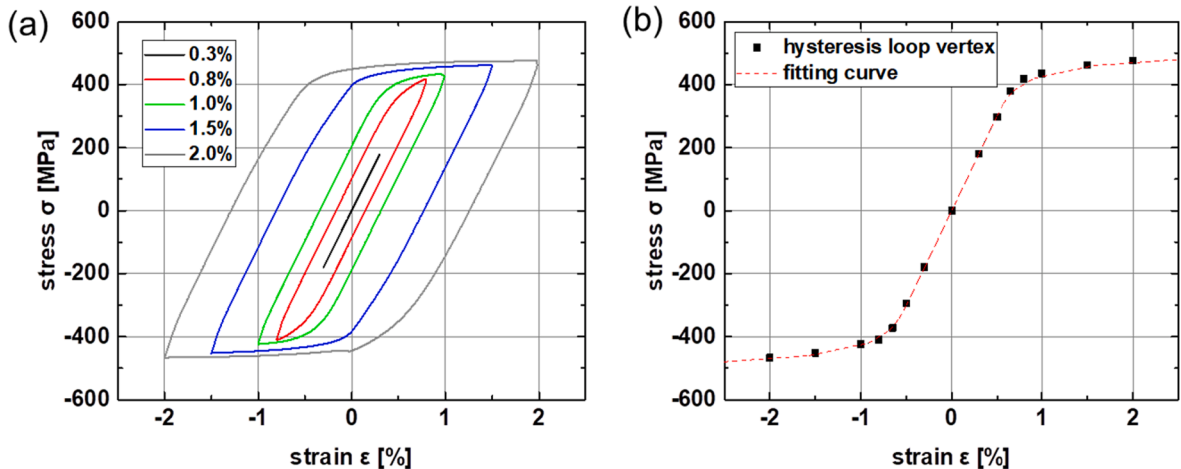

Fig. 8. (a) The simulated hysteresis loop (b) the stabilized cyclic stress versus strain.
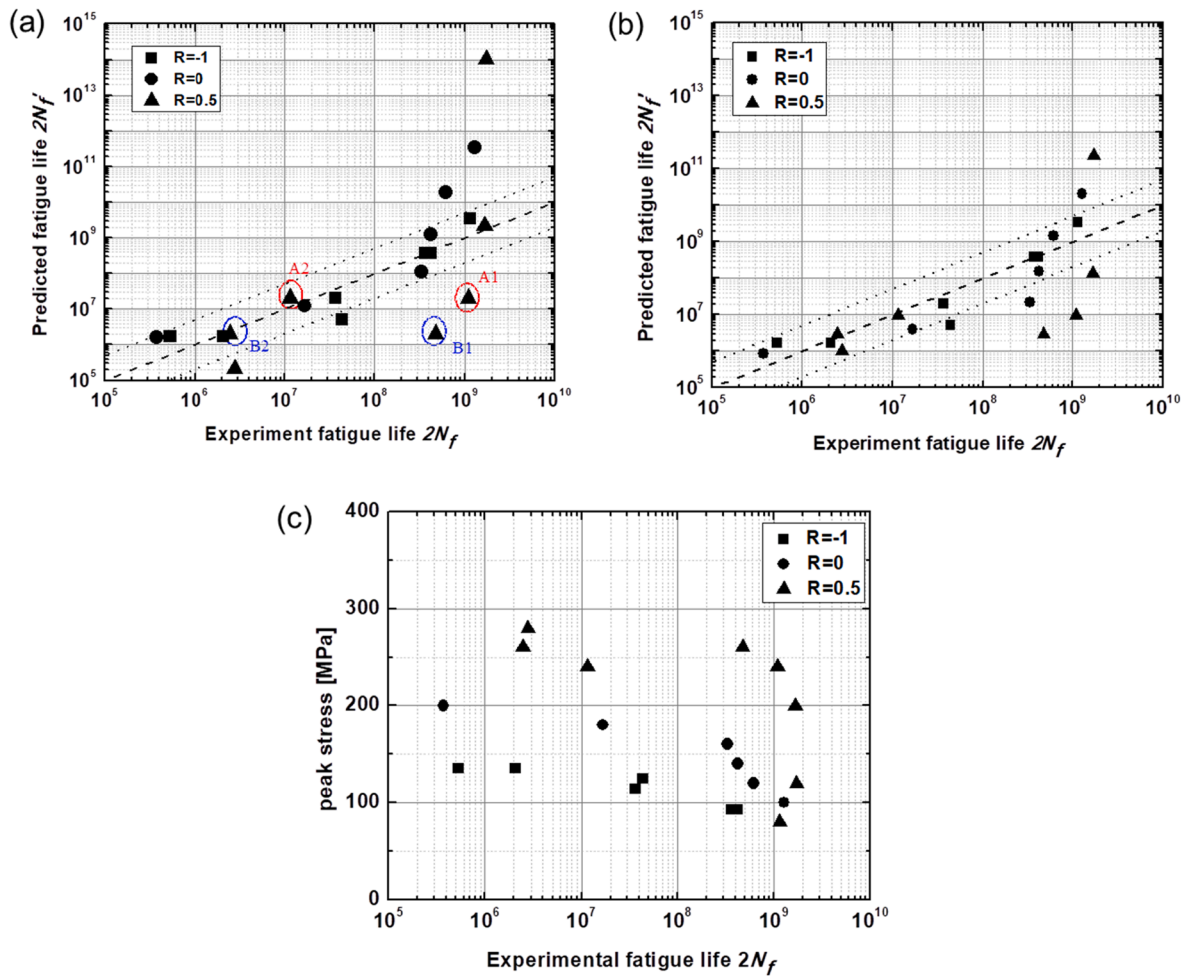
Fig. 9. (a) Comparison of Morrow's model predicted life against experiment fatigue life; (b) Comparison of SWT model predicted life versus experiment fatigue life; (c) experimental peak stress versus experiment fatigue life.

Table 3
Fatigue test data of stress level versus life cycles.

Specimen No.	Stress amplitude (MPa)	Stress ratio R	Mean stress (MPa)	Fatigue life (cycles)
1	114	−1	0	3.70E+07
2	135	−1	0	5.31E+05
3	125	−1	0	4.40E+07
4	135	−1	0	2.07E+06
5	93	−1	0	4.20E+08
6	93	−1	0	3.67E+08
7	80	−1	0	1.15E+09
8	50	0	50	1.28E+09
9	100	0	100	3.72E+05
10	70	0	70	4.23E+08
11	80	0	80	3.32E+08
12	60	0	60	6.22E+08
13	90	0	90	1.68E+07
14	30	0.5	90	1.73E+09
15	60	0.5	180	1.16E+07
16	50	0.5	150	1.67E+09
17	60	0.5	180	1.10E+09
18	70	0.5	210	2.79E+06
19	65	0.5	195	4.74E+08
20	65	0.5	195	2.48E+06

above four specimens were shown in Fig. 10. It can be seen that the crack initiation site of A$_2$ was at the specimen surface (Fig. 10(b)), whereas the crack initiation site of A$_1$ was located in the internal of specimen (Fig. 10(a)) due to the smaller surface defects, which rationalized the unusually

long fatigue life of Specimen A$_1$. For Specimen B$_1$ and B$_2$. It is similar that the long fatigue life of Specimen B$_1$ was related to the internal crack initiation site against the surface crack initiation mode of B$_2$, as shown in Fig. 9(c) and (d). The above observation suggested a tendency of transition from surface crack initiation to subsurface or internal crack initiation with increasing fatigue life. Similar trend has also been reported in previous studies [14].

Additionally, in Fig. 9 (a) and (b) it can be seen that the two models cannot provide conservative prediction when the fatigue life exceeds 10^9 cycles. And the non-conservation is more evident in the prediction using Morrow's model. The life prediction error can be defined as follows:

$$\text{error} = log_{10}N_f^{'} - log_{10}N_f \tag{14}$$

where N_f is the experimental fatigue life, and $N_f^{'}$ is the predicted life under the same loading condition. If the error is positive, the predicted life is not conservative. If the error is negative, the predicted life is relatively conservative. It is found that the fatigue life prediction error in this study follows the normal distribution. The probability density functions of normal distribution corresponding to Morrow's model and SWT model are shown in Fig. 11.

The result of Morrow's model prediction had a positive expectation, which indicated that the model was not conservative in the prediction of fatigue life. The result of SWT model was negative, indicating that the prediction with SWT model was relatively conservative. On the other hand, the normal distribution curve of Morrow's model is relatively flat,
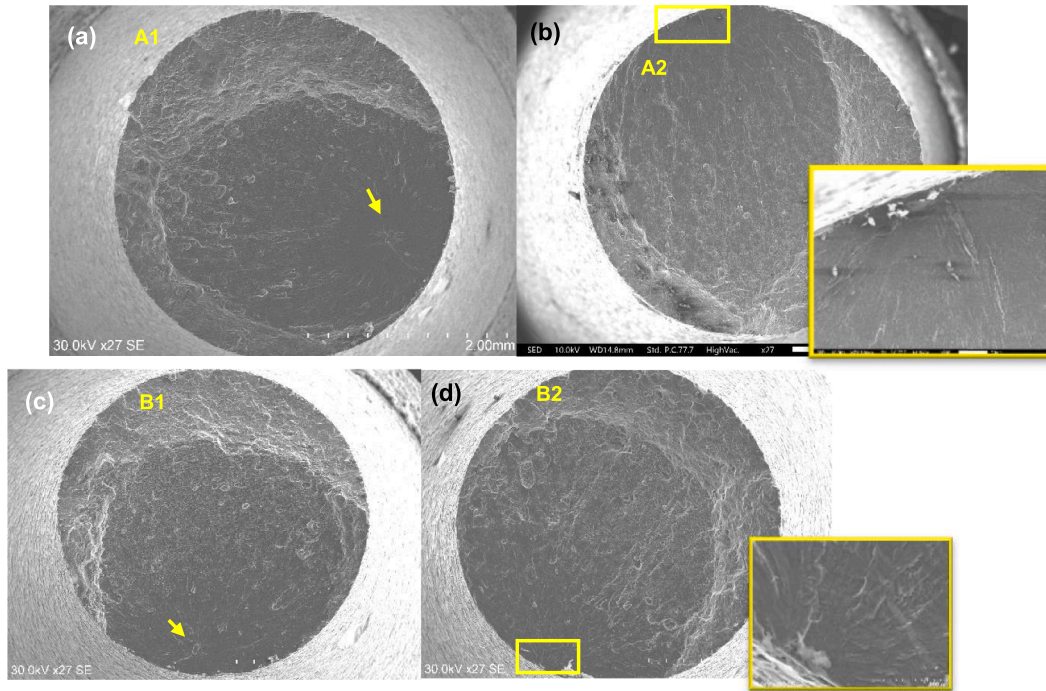
Fig. 10. Fatigue fracture surfaces of specimens: (a) Specimen A$_1$, σ_{max} = 240 MPa, R = 0.5, N_f = 1.10 × 10^9 cycles; (b) Specimen A$_2$, σ_{max} = 240 MPa, R = 0.5, N_f = 1.16 × 10^7 cycles; (c) Specimen B$_1$, σ_{max} = 260 MPa, R = 0.5, N_f = 4.74 × 10^8 cycles; (d) Specimen B$_2$, σ_{max} = 260 MPa, R = 0.5, N_f = 2.48 × 10^6 cycles.
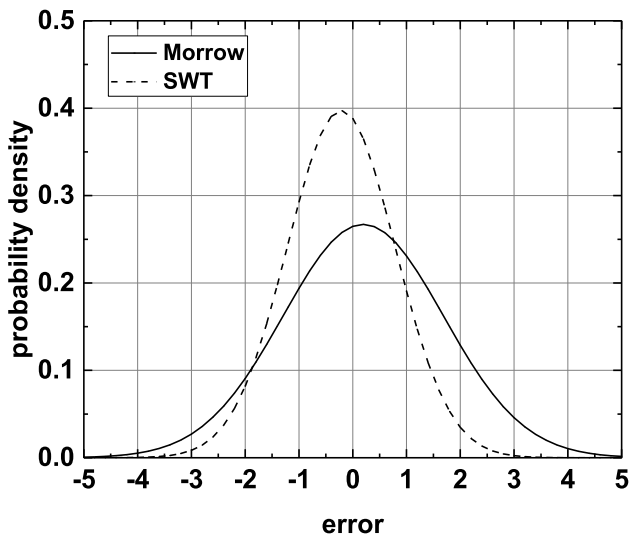

Fig. 11. Normal distribution of fatigue life prediction error of Morrow's model and SWT model.

indicating that the variation of the predicted fatigue life is large. In contrast, the normal distribution curve of SWT was narrow and its variation is relatively small, so the fatigue life prediction with SWT model was more accurate and reliable. In summary, the prediction of fatigue life by SWT model is in good agreement with the fatigue test results in the range between 10^5 and 10^9. Therefore, SWT model is recommended for fatigue life evaluation of SLMed AlSi10Mg in HCF and VHCF regimes.

In addition, as the fatigue loading cycles exceeded 10^9, the SWT model became less accurate in the fatigue life prediction in the HCF and VHCF regimes. The underlying reason may be that the crystal plasticity model with Voronoi elements did not take into account the effects of defects in the AlSi10Mg alloy. Pores and inclusions were reported to be

the primary defects observed in the AlSi10Mg alloy specimens made by SLM [42–46]. These defects were also observed in the present alloy under scanning electronic microscope, as shown in the micrographs in Fig. 12. Statistical analysis of all pores on fracture surfaces and metallographs suggested an average diameter of 70 μm for pores. For inclusion, it is also simplified as circular shape. According to the statistical results of inclusion dimensions, the average diameter of inclusion is about 50 μm.

4.2. Plastic strain around pores and inclusions

Voronoi elements with a pore or an inclusion were used for the finite element simulation, as shown in Fig. 6. Cyclic loading was applied at the upper boundary of the polycrystalline aggregate along the vertical (y-axis) direction with a strain amplitude of 0.2%. According to the previous studies in literature [47], accumulated plastic shear strain is closely related to the crack initiation process and hence can be used to quantify the fatigue crack initiation life under cyclic loading. The accumulated plastic shear strain is defined as:

$$p_{acc} = \int_0^t \sqrt{\frac{2}{3}\boldsymbol{L}_p : \boldsymbol{L}_p} d\tau \qquad (15)$$

The accumulated plastic shear strain, denoted as SDV121 in the following figures and paragraphs, was evidently enhanced near the defects, such as pores or inclusions, as shown in Fig. 13. Fig. 13(a) shows the contour of accumulated plastic shear strain for the Voronoi polycrystalline model with no defects. The strain distribution is overall inhomogeneous in different grains due to different crystal orientations. The strain hotspot appeared at the grain boundaries and the maximum plastic shear strain value was about 8.15 × 10^{-3}.

For the Voronoi model with a pore, the contour of accumulated plastic shear strain is shown in Fig. 13(b). Evident strain concentration was observed near the pore, indicating that the plastic strain is much smaller in the other regions compared with the pore. It is consistent with the observed crack initiation from a pore on the fracture surface in Fig. 12(a). The maximal accumulated shear strain occurred on the
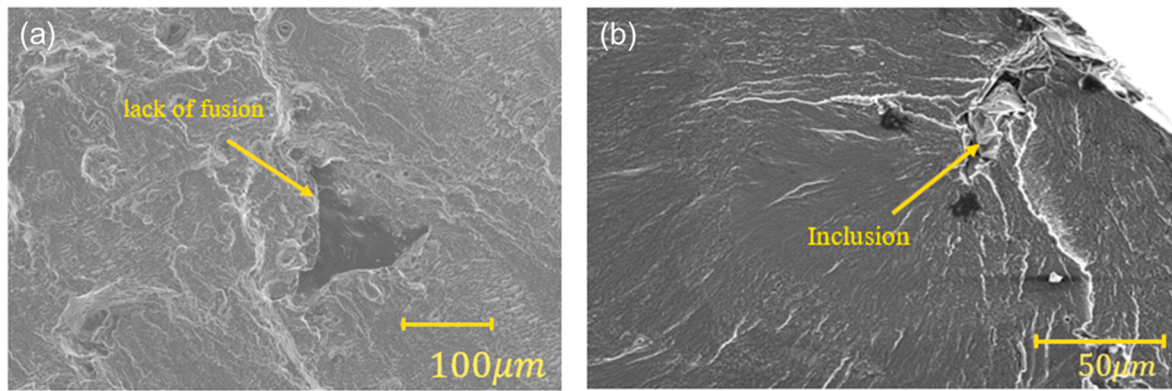
Fig. 12. The defects in the present AlSi10Mg alloy examined by scanning electronic microscope: (a) internal pore; (b) subsurface inclusion (the loading direction is perpendicular to the fracture surface).
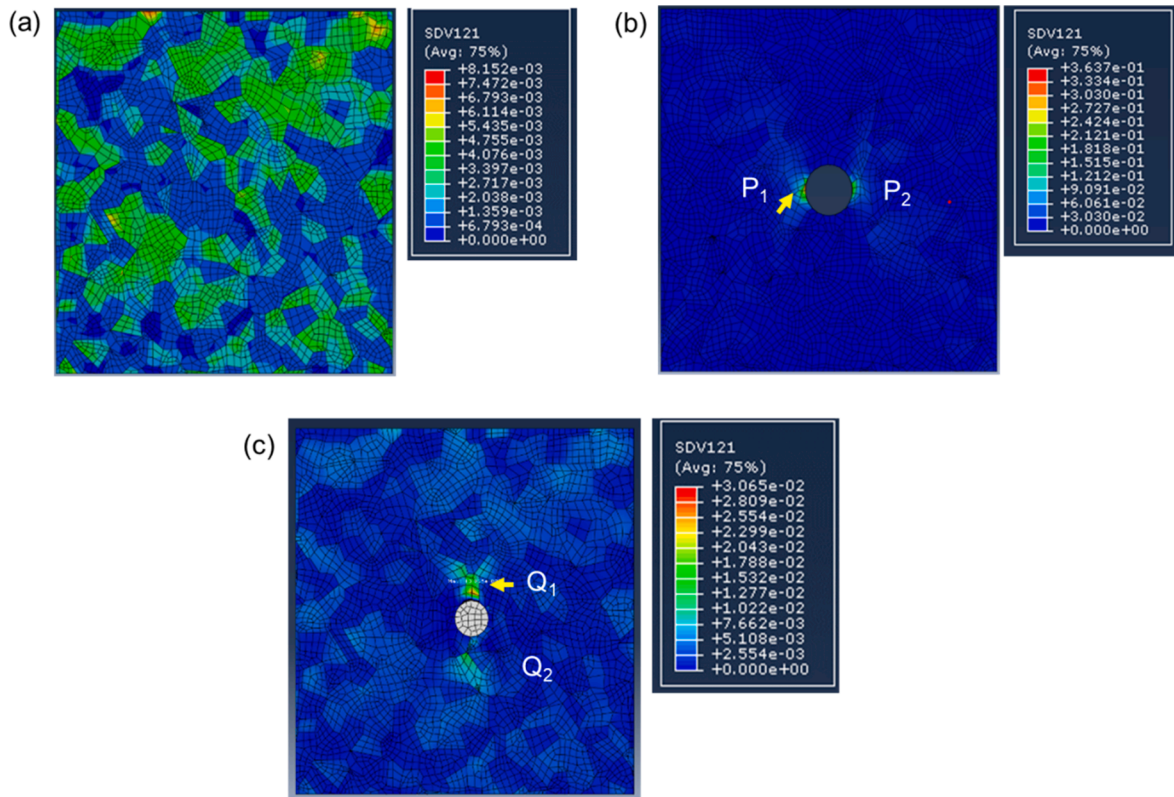

Fig. 13. Accumulated plastic shear strain contour of (a) Voronoi polycrystalline model with no defects (b) Voronoi polycrystalline model with a pore (c) Voronoi polycrystalline model with an inclusion (The loading direction is along vertical. SDV121 represents accumulated plastic shear strain).

horizontal side of the circular pore, perpendicular to the loading direction. It is reasonable because the pore can be regarded as a special case of non-sharp crack. In this case, the region P1 and P2 act as the blunt crack tip, hence they are the region representing the largest stress concentration.

For the case of inclusion, as shown in Fig. 13 (c), the accumulated shear strain is also evidently concentrated around the inclusion, due to larger stiffness of inclusion. In the region far away from the inclusion, the distribution of accumulated shear strain in different grains is similar to that in Fig. 13(a). It is also noticed that the concentration of accumulated shear strain due to an inclusion is less remarkable than that due to a pore. Similar effects have been also reported in recent studies on martensitic steels by Prasannavenkatesan et al. [48]. They suggested that a pore can be treated as a special compliant inclusion with a local free-surface effect, which leads to local softening.

Moreover, for the case of inclusion, the hotspot of strain map, i.e. the maximal accumulated shear strain, appeared at the vertical side of the inclusion. It should be noticed that the location of hotspot in Fig. 13(c) is different from that in Fig. 13 (b). For inclusion in Fig. 13(c), the stiff inclusion was less deformable than the matrix, so the matrix would afford more strain as the total elongation or tensile strain of the entire model was predefined. Hence the adjacent region of inclusion, i.e. Q1 and Q2, would be subjected to higher tensile strain than nominal, leading to evident deformation localization. The above result is consistent with the previous simulation study conducted by Pineau and Forest [49].

Fig. 14(a) shows the variation of accumulated plastic shear strain for Voronoi polycrystalline model with a pore under cyclic loading. SDV121 represents the accumulated plastic shear strain. The red line in Fig. 14(a) represents the maximum value of accumulated plastic shear strain of

Voronoi model with a pore (corresponding to Fig. 13(b)). The blue line represents the maximum accumulated shear strain of the Voronoi model with no defects (corresponding to Fig. 13(a)). The triangle wave shape in Fig. 14(a) is used for the cyclic loading, with the solid line meaning tension, and the dotted line meaning compression. It is evident that the accumulated plastic shear strain increased gradually under cyclic loading, and the increment per cycle decreased gradually. According to the study of Gillner and Münstermann [50,51], the increment of local accumulated plastic shear strain kept almost constant after the first cycle. Hence, if a constant increment of accumulated plastic shear strain was assumed in this study, the plastic strain will be overestimated and a conservation prediction of crack initiation life will be obtained [25]. From Fig. 14 (b), it can be seen that after 10 cycles of loading, the maximum accumulated shear strain near the pore increased by 2 orders of magnitude and stabilized, in contrast with the Voronoi model with no defects. Considering that the accumulated shear strain is related to the fatigue crack initiation life as suggested by McDowell et al. [25], porosity plays an important role in the HCF life of SLMed AlSi10Mg alloy.

Fig. 15 shows the variation of accumulated plastic shear strain for Voronoi polycrystalline model with an inclusion under cyclic loading. The red line in Fig. 15(a) represents the maximum value of accumulated plastic shear strain (corresponding to Fig. 13(c)). The blue line represents the maximum accumulated shear strain of the Voronoi model with no defects (corresponding to Fig. 13 a). It is evident that the maximum accumulated plastic shear strain with an inclusion (red line) is larger than that with no defects (blue line), and the difference is about an order of magnitude. It is indicated that the concentration of accumulated shear strain due to inclusions is less pronounced than that due to pores. Considering that pores are commonly formed during the SLM process, the porosity is a key influence factor that can be optimized to improve the HCF and VHCF life of SLMed alloys. In the present study, the dimensions of pores or inclusions were chosen based on SEM observations and the shapes were idealized as circular for the ease of comparative analysis base on crystal plasticity simulation. Existing research [50] revealed that inclusion size had a significant influence on fatigue life, followed by shape, and surface roughness. For instance, the shape ratio of the pores and inclusions will affect the stress concentration around the defects and hence alter the localized plastic strain. These factors of pores and inclusions should be further studied in future work.

4.3. Effect of residual stresses on fatigue life

The crystal plasticity finite element model with Voronoi grains with an embedded inclusion was cooled down from 225 °C to 175 °C. The stress distribution in the grains after cooling down is shown in Fig. 16. It
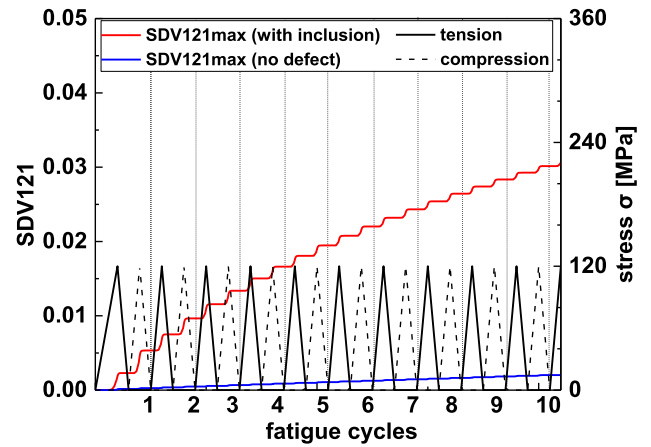

Fig. 15. The accumulated plastic shear strain variation with influence of an inclusion.

is shown that the cooling process introduced evident residual stresses at the interface between the inclusion and the matrix. In the region far away from the inclusion, the residual stress in the AlSi10Mg matrix was
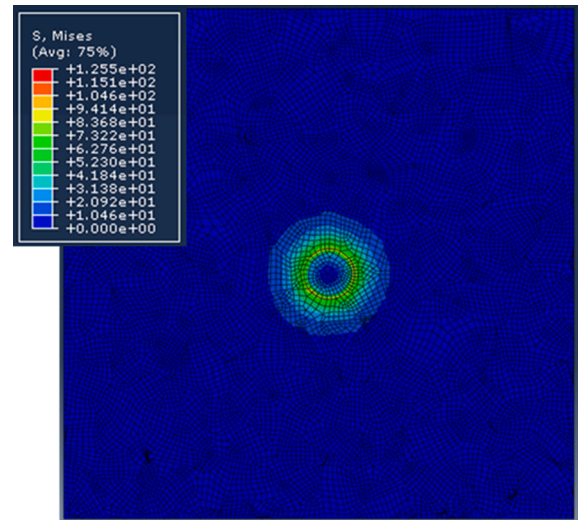

Fig. 16. The distribution of residual stresses around the inclusion after cooling from 225 °C to 175 °C.
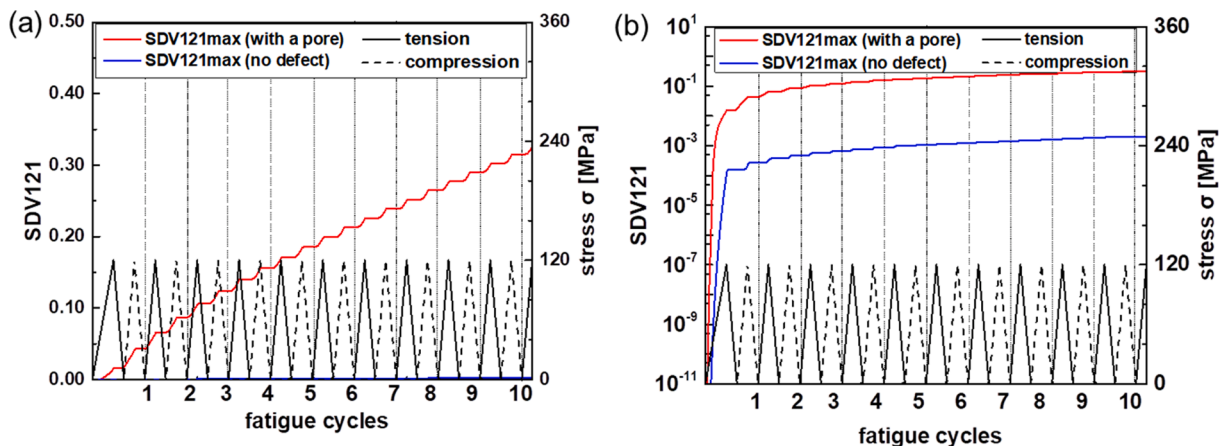

Fig. 14. The variation of accumulated plastic shear strain under cyclic loading with the influence of a pore: (a) linear y-axis (b) logarithmic y-axis (SDV121 represents accumulated plastic shear strain).

negligible. While approaching the inclusion/matrix interface, the residual stress increased gradually and reached the maximum at the interface, as shown in Fig. 16. The calculated residual stress in Fig. 16 is close to the residual stress of 150 MPa reported in similar AlSi10Mg alloys manufactured by selective laser melting [46].

Fig. 17(a) shows the accumulated plastic shear strain of a Voronoi model without cooling under cyclic loading of 120 MPa for 5 cycles. In Fig. 17(b), the alloy was cooled down from 225 °C to 175 °C and then subjected to 120 MPa cyclic loading. It is shown that the maximum accumulated plastic shear strain occurred at the same location but the value was evidently increased by 10%. In Fig. 17(c), the alloy was cooled down from 225 °C to 25 °C and then subjected to 120 MPa cyclic loading. It is shown that the distribution of accumulated plastic shear strain changed slightly and the maximum strain value was increased by 22% than that of Fig. 17(a). The increased plastic strain was closely related to the larger residual stress generated during the cooling process.

For the case without cooling, the hot spot of the accumulated plastic strain map in Fig. 17(a) appear at the upper and lower region of the inclusion, similar to that in Fig. 13(c). The maximum strain concentration region has a small distance from the interface between the inclusion and matrix. Fig. 17(b) showed similar result as that in Fig. 17(a). However, for the specimen cooled by 200 °C (Fig. 17(c)), the accumulated plastic strain achieved the maximum value near the inclusion-matrix interface, about 45° off the loading axis, shown in Fig. 17 (c). In Fig. 17, it is shown that the strain hot spots exhibited two types of concentration. For the first type (Fig. 17(a) and (b)), the strain concentration regions were similar to the previous studies by Fleming and

Temis [52], known as the frontal zone. For the second type, the strain concentration region (Fig. 17(c)) is similar to the simulation results of Pineau and Forest [49]. The two types of strain concentration regions shown above would act as the preferential location for fatigue crack initiation.

Fig. 18 shows the variation of accumulated plastic shear strain versus cooling process and fatigue loading cycles for the three cases. The left side of the vertical dotted line represents the cooling process, and the right side of the vertical dotted line represents the cyclic loading process. While there was a large temperature drop, e.g. 200 °C, the cooling process would introduce evident accumulated shear strain. After the first cyclic loading, the accumulated shear strain greatly increased, and the increment magnitude in the material cooled down by 200 °C was larger than that cooled by 50 °C. After the first cycle of loading, the plastic shear strain accumulated rapidly. This phenomenon was known to be associated with the release of residual stresses. Taking the case of cooling down by 200 °C as example, the initial maximum residual stress was about 300 MPa as shown in Fig. 19 (a). After the first cyclic loading, the residual stress dropped to about 255 MPa as shown in Fig. 19 (b), about 17% decrease of residual stress, similar to that reported by Gu et al. [27]. The residual stress was released while a large accumulated plastic shear strain was generated. In the following loading cycles, the residual stress remained almost unchanged and got stabilized at around 250 MPa as shown in Fig. 19 (c).

The first few loading cycles would release the residual stresses in the material to a certain extent and brought cumulative plastic strain into the local neighborhood of inclusion. The larger the residual stress was,
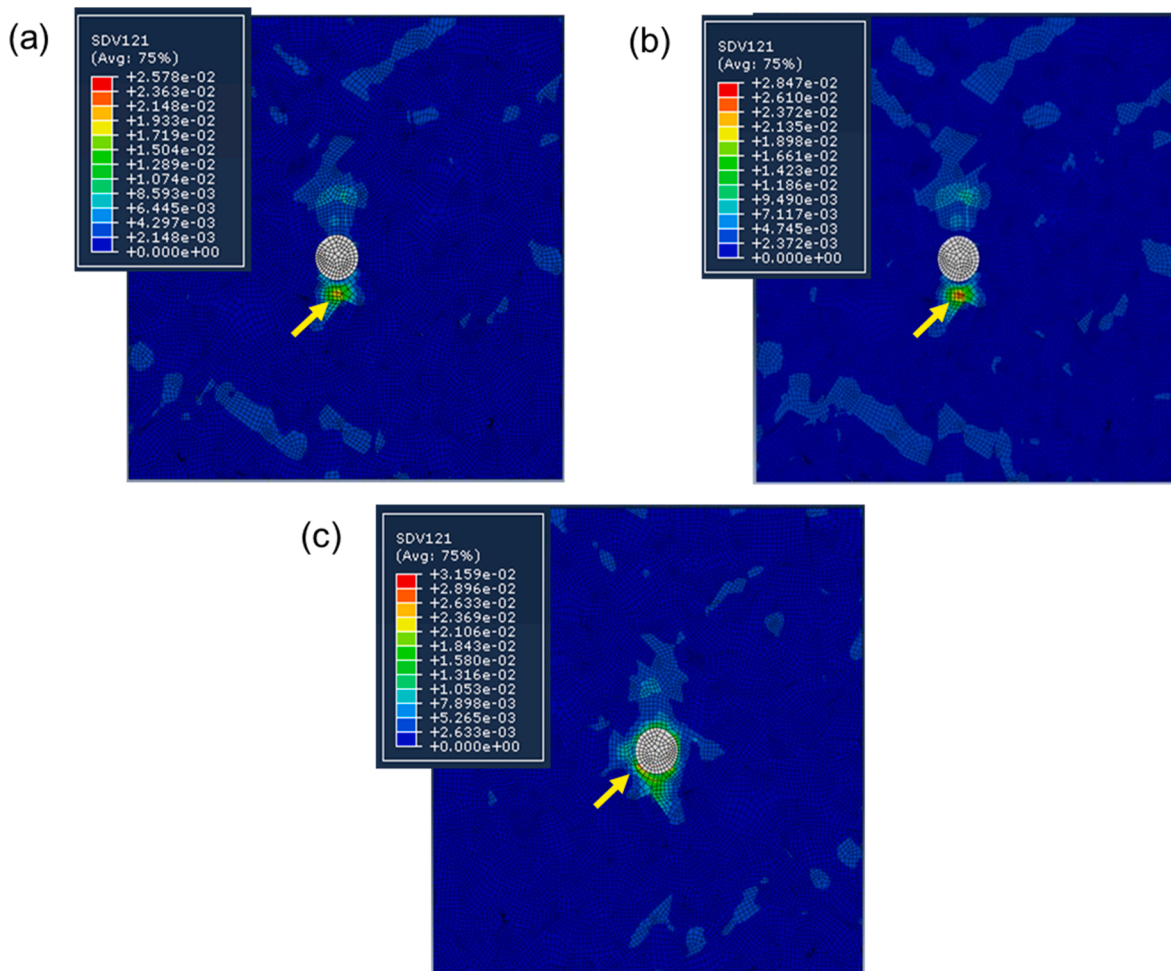

Fig. 17. Distribution of accumulated plastic shear strain in the AlSi10Mg alloy (a) without cooling, (b) cooling from 225 °C to 175 °C, (c) cooling from 225 °C to 25 °C (The loading direction is along vertical. SDV121 represents accumulated plastic shear strain).
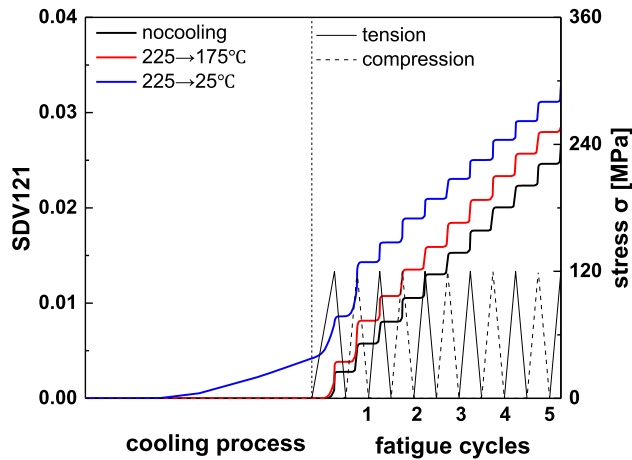
Fig. 18. Variation of accumulated shear strain with different cooling process induced residual stress conditions.

the larger the increment of accumulated shear strain was. In this case, it would facilitate the crack initiation process, and hence shorten the fatigue life of the alloy in the HCF and VHCF regimes. The accumulated plastic shear strain showed obvious difference when the residual stress is considered, which would lead to different predicted fatigue life. A

comparative study was performed in the work of Gu et al. [27]. By using the formula proposed by McDowell et al. [25], they conducted fatigue life prediction, suggesting that the simulation considering residual stress showed better agreement with experiment result than that neglecting residual stress effect. The residual stress kept almost constant after the relaxation in the first several cycles, as shown in Fig. 19(c). Hence, the present study suggested two roles of residual stress in affecting fatigue life: (i) the constant part of residual stress remained after relaxation; (ii) the accumulated plastic strain generated while the residual stress partially relaxed. A recent study [53] introduced the residual stress in fatigue indication parameter for the sake of life prediction. In the present study, it is possible to replace engineering strain by accumulated plastic shear strain in Morrow's model or SWT model and the residual stress can be considered as mean stress in the fatigue life model for the convenience of engineering application. Both the present study and the work of Gu et al. [27] have indicated the importance of taking into account the residual stress associated with inclusion while studying the fatigue life of SLMed alloy. Future work should focus on quantification of the variation of residual stress during cyclic loading, its uniformity in material, and multi-axial effects etc. while developing fatigue life prediction model with residual stress effects.

5. Conclusions

In the present study, the crystal plasticity finite element model with Voronoi aggregates was used to study the HCF and VHCF properties of
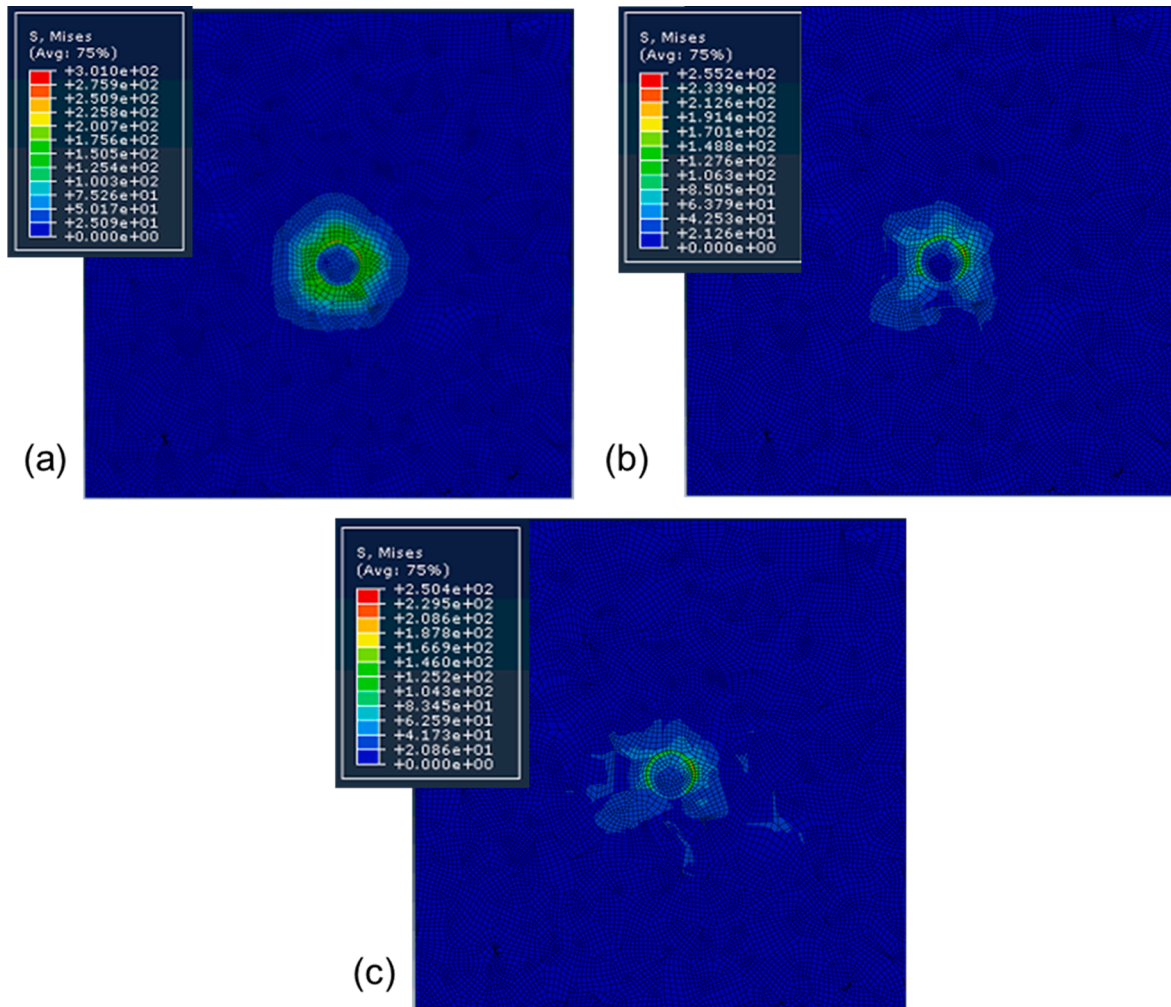

Fig. 19. The distribution of residual stresses in the material cooling by 200 °C under (a) 0 cycle, (b) 1 cycle, and (c) 15 cycles of loading (The loading direction is along vertical).

AlSi10Mg alloy fabricated by SLM. The following conclusions have been obtained:

1) The fatigue life of AlSi10Mg alloy predicted by the SWT model is in good agreement with the experimental results between 10^5 and 10^9 cycles. In the HCF and VHCF regimes, fatigue life highly depends on the defect characteristics of the alloy, such as inclusions and pores.

2) The accumulated plastic shear strain is evidently increased near the defects, such as pores and inclusions, which would accelerate the crack initiation process and thus shorten the fatigue life. Moreover, it is shown that a pore has more significant effect on strain localization than that of an inclusion. The maximum accumulated plastic slip occurred at different locations for a Voronoi model containing a pore compared with that containing an inclusion, due to the compatibility of deformation.

3) The residual stress near an inclusion is harmful to the fatigue life of AlSi10Mg alloy. In the first several loading cycles, the residual stress would be partially released, accompanied with evident accumulated plastic shear strain generated nearby. Both aspects would facilitate the fatigue crack initiation process and reduce the fatigue life of AlSi10Mg alloy.

Declaration of Competing Interest

The authors declare that they have no known competing financial interests or personal relationships that could have appeared to influence the work reported in this paper.

Acknowledgements

References

[1] Frazier WE. Metal additive manufacturing: a review. J Mater Eng Perform 2014;23: 1917–28.

[2] Suryawanshi J, Prashanth K, Scudino S, Eckert J, Prakash O, Ramamurty U. Simultaneous enhancements of strength and toughness in an Al-12Si alloy synthesized using selective laser melting. Acta Mater 2016;115:285–94.

[3] Rafi H, Karthik N, Gong H, Starr TL, Stucker BE. Microstructures and mechanical properties of Ti6Al4V parts fabricated by selective laser melting and electron beam melting. J Mater Eng Perform 2013;22:3872–83.

[4] Leuders S, Thöne M, Riemer A, Niendorf T, Tröster T, Richard Ha, Maier H. On the mechanical behaviour of titanium alloy TiAl6V4 manufactured by selective laser melting: fatigue resistance and crack growth performance. Int J Fatigue 2013;48: 300–7.

[5] Li XP, Ji G, Chen Z, Addad A, Wu Y, Wang H, et al. Selective laser melting of nano-TiB2 decorated AlSi10Mg alloy with high fracture strength and ductility. Acta Mater 2017;129:183–93.

[6] Siddique S, Awd M, Tenkamp J, Walther F. Development of a stochastic approach for fatigue life prediction of AlSi12 alloy processed by selective laser melting. Eng Fail Anal 2017;79:34–50.

[7] Siddique S, Awd M, Tenkamp J, Walther F. High and very high cycle fatigue failure mechanisms in selective laser melted aluminum alloys. J Mater Res 2017;32: 4296–304.

[8] Aboulkhair NT, Everitt NM, Ashcroft I, Tuck C. Reducing porosity in AlSi10Mg parts processed by selective laser melting. Addit Manuf 2014;1:77–86.

[9] Major JF, Alcan R. Aluminum and aluminum alloy castings. ASM Handbook Volume 15: Casting; 2008, p. 1059–84.

[10] Srinivas M, Babu BS. A critical review on recent research methodologies in additive manufacturing. Mater Today: Proc 2017;4:9049–59.

[11] Hong Y, Sun C. The nature and the mechanism of crack initiation and early growth for very-high-cycle fatigue of metallic materials – An overview. Theor Appl Fract Mec 2017;92:331–50.

[12] Kikukawa KOM, Ogura K. Push-pull fatigue strength of mild steel at very high frequencies of stress up to 100 kc/s. J Basic Eng 1965;87:857–964.

[13] Wells Joseph M. First international conference on fatigue and corrosion fatigue up to ultrasonic frequencies. JOM 1982;34(6):33–6. https://doi.org/10.1007/BF03338024.

[14] Lankford J, Kusenberger F. Initiation of fatigue cracks in 4340 steel. Metall Trans 1973;4:553–9.

[15] Emura H, Asami K. Fatigue strength characteristics of high strength steel. Trans Jpn Soc Mech Eng, A 1989;55:45–50.

[16] Sakai T, Takeda M, Shiozaka K, Ochi Y, Nakajima M. Experimental reconfirmation of characteristic SN property for high carbon chromium bearing steel in wide life region in rotating bending. Zairyo 2000;49:779–85.

[17] Hong Y, Zhao A, Qian G, Zhou C. Fatigue strength and crack initiation mechanism of very-high-cycle fatigue for low alloy steels. Metall Mater Trans A 2012;43: 2753–62.

[18] Hong Y, Liu X, Lei Z, Sun C. The formation mechanism of characteristic region at crack initiation for very-high-cycle fatigue of high-strength steels. Int J Fatigue 2016;89:108–18.

[19] Wang Q, Berard J, Rathery S, Bathias C. Technical note High-cycle fatigue crack initiation and propagation behaviour of high-strength sprin steel wires. Fatigue Fract Eng M 1999;22:673–7.

[20] Khanzadeh M, Tian W, Yadollahi A, Doude HR, Tschopp MA, Bian L. Dual process monitoring of metal-based additive manufacturing using tensor decomposition of thermal image streams. Addit Manuf 2018;23:443–56.

[21] Hennessey C, Castelluccio GM, McDowell DL. Sensitivity of polycrystal plasticity to slip system kinematic hardening laws for Al 7075–T6. Mat Sci Eng A 2017;687: 241–8.

[22] Bridier F, McDowell DL, Villechaise P, Mendez J. Crystal plasticity modeling of slip activity in Ti–6Al–4V under high cycle fatigue loading. Int J Plasticity 2009;25: 1066–82.

[23] Zhang M, Zhang J, McDowell D. Microstructure-based crystal plasticity modeling of cyclic deformation of Ti–6Al–4V. Int J Plasticity 2007;23:1328–48.

[24] Patra A, Priddy MW, McDowell DL. Modeling the effects of microstructure on the tensile properties and micro-fracture behavior of Mo–Si–B alloys at elevated temperatures. Intermetallics 2015;64:6–17.

[25] Castelluccio GM, Musinski WD, McDowell DL. Computational micromechanics of fatigue of microstructures in the HCF–VHCF regimes. Int J Fatigue 2016;93: 387–96.

[26] Han S, Yang X, Shi D, Miao G, Huang J, Li R. Microstructure-sensitive modeling of competing failure mode between surface and internal nucleation in high cycle fatigue. Int J Plasticity 2020;126:102622.

[27] Gu C, Lian J, Bao Y, Münstermann S. Microstructure-based fatigue modelling with residual stresses: prediction of the microcrack initiation around inclusions. Mat Sci Eng A 2019;751:133–41.

[28] Takata N, Liu M, Kodaira H, Suzuki A, Kobashi M. Anomalous strengthening by supersaturated solid solutions of selectively laser melted Al–Si-based alloys. Addit Manuf 2020;33.

[29] Cai G, Li C, Wang D, Zhou Y. Investigation of annealing temperature on microstructure and texture of Fe-19Cr-2Mo-Nb-Ti ferritic stainless steel. Mater Charact 2018;141:169–76.

[30] Romano S, Patriarca L, Foletti S, Beretta S. LCF behaviour and a comprehensive life prediction model for AlSi10Mg obtained by SLM. Int J Fatigue 2018;117:47–62.

[31] Ma X, Wei D, Han Q, Rui S, Su D, Yang W, et al. Parametric study of cyclic plasticity behavior in a directionally solidified superalloy with partial recrystallization by crystal plasticity finite element simulation. J Mater Eng Perform 2019;28:3332–40.

[32] Ma X, Zhai HL, Zuo L, et al. Fatigue short crack propagation behavior of selective laser melted Inconel 718 alloy by in-situ SEM study: influence of orientation and temperature. Int J Fatigue 2020;139:105739.

[33] Ma X, Wei D, Allison JE, Wang B. Integrated computational materials engineering simulation studies of nuclear alloys based on crystal plasticity modeling (in Chinese). Scientia Sinica - Phys, Mech & Astron 2019;46. https://doi.org/10.1360/SSPMA-2019-0121.

[34] Proudhon H, Li J, Wang F, Roos A, Chiaruttini V, Forest S. 3D simulation of short fatigue crack propagation by finite element crystal plasticity and remeshing. Int J Fatigue 2016;82:238–46.

[35] Rovinelli A, Sangid MD, Proudhon H, Guilhem Y, Lebensohn RA, Ludwig W. Predicting the 3D fatigue crack growth rate of small cracks using multimodal data via Bayesian networks: in-situ experiments and crystal plasticity simulations. J Mech Phys Solids 2018;115:208–29.

[36] Yue ZF. Surface roughness evolution under constant amplitude fatigue loading using crystal plasticity. Eng Fract Mech 2005;72:749–57.

[37] Musinski WD, McDowell DL. Microstructure-sensitive probabilistic modeling of HCF crack initiation and early crack growth in Ni-base superalloy IN100 notched components. Int J Fatigue 2012;37:41–53.

[38] Bathias C. There is no infinite fatigue life in metallic materials. Fatigue Fract Eng Mater Struct 1999;22:559–65.

[39] Caton MJ, Jones JW, Mayer H, Stanzl-Tschegg SE, Allison JE. Demonstration of an endurance limit in cast 319 aluminum. Metall Mater Trans A 2003;34A:33–41.

[40] Li L, Shen L, Proust G. Fatigue crack initiation life prediction for aluminum alloy 7075 using crystal plasticity finite element simulations. Mech Mater 2015;81: 84–93.

[41] Cailletaud G, Forest S, Jeulin D, Feyel F, Galliet I, Mounoury V, et al. Some elements of microstructural mechanics. Comp Mater Sci 2003;27:351–74.

[42] Qian G, Jian Z, Pan X, Berto F. In-situ investigation on fatigue behaviors of Ti-6Al-4V manufactured by selective laser melting. Int J Fatigue 2020;133:105424.

[43] Qian G, Li Y, Tridello A, Paolino D, Berto F, Hong Y. Very-high-cycle fatigue behavior of Ti-6Al-4V manufactured by selective laser melting: Effect of build orientation. Int J Fatigue 2020;136:105628.

[44] Qian G, Zhou C, Hong Y. Experimental and theoretical investigation of environmental media on very-high-cycle fatigue behavior for a structural steel. Acta Mater 2011;59:1321–7.

[45] Qian G, Lei W. A statistical model of fatigue failure incorporating effects of specimen size and load amplitude on fatigue life. Philos Mag 2019;99:2089–125.

[46] Qian G, Jian Z, Qian Y, Pan X, Ma X, Hong Y. Very-high-cycle fatigue behavior of AlSi10Mg manufactured by selective laser melting: effect of build orientation and mean stress. Int J of Fatigue 2020;105696.

[47] Manonukul A, Dunne F. High–and low–cycle fatigue crack initiation using polycrystal plasticity. Proc R Soc London Ser A Mat 2004;460:1881–903.

[48] Prasannavenkatesan R, Przybyla CP, Salajegheh N, McDowell DL. Simulated extreme value fatigue sensitivity to inclusions and pores in martensitic gear steels. Eng Fract Mech 2011;78:1140–55.

[49] Pineau A, Forest S. Effects of inclusions on the very high cycle fatigue behaviour of steels. Fatigue Fract Eng M 2017;40:1694–707.

[50] Gillner K, Münstermann S. Numerically predicted high cycle fatigue properties through representative volume elements of the microstructure. Int J Fatigue 2017;105:219–34.

[51] Gillner K, Henrich M, Münstermann S. Numerical study of inclusion parameters and their influence on fatigue lifetime. Int J Fatigue 2018;111:70–80.

[52] Fleming W, Temis J. Numerical simulation of cyclic plasticity and damage of an aluminium metal matrix composite with particulate SiC inclusions. Int J Fatigue 2002;24:1079–88.

[53] Li Y, Chen J, Wang J, Shi X, Chen L. Study on the effect of residual stresses on fatigue crack initiation in rails. Int J Fatigue 2020;139.